

Sub-micron silica diaphragm-based fiber-tip Fabry–Perot interferometer for pressure measurement

Changrui Liao,¹ Shen Liu,¹ Lei Xu,² Chao Wang,^{1,3} Yiping Wang,^{1,*} Zhengyong Li,¹ Qiao Wang,¹ and D. N. Wang³

¹Key Laboratory of Optoelectronic Devices and Systems of Ministry of Education and Guangdong Province, College of Optoelectronic Engineering, Shenzhen University, Shenzhen 518060, China

²Department of Computing, The Hong Kong Polytechnic University, Hong Kong, China

³Department of Electrical Engineering, The Hong Kong Polytechnic University, Hong Kong, China

*Corresponding author: ypwang@szu.edu.cn

Received January 23, 2014; revised April 2, 2014; accepted April 7, 2014;
posted April 8, 2014 (Doc. ID 205172); published May 2, 2014

We demonstrate a sub-micron silica diaphragm-based fiber-tip Fabry–Perot interferometer for pressure sensing applications. The thinnest silica diaphragm, with a thickness of ~ 320 nm, has been achieved by use of an improved electrical arc discharge technique. Such a sub-micron silica diaphragm breaks the sensitivity limitation imposed by traditional all-silica Fabry–Perot interferometric pressure sensors and, as a result, a high pressure sensitivity of ~ 1036 pm/MPa at 1550 nm and a low temperature cross-sensitivity of ~ 960 Pa/°C are achieved when a silica diaphragm of ~ 500 nm in thickness is used. Moreover, the all-silica spherical structure enhanced the mechanical strength of the micro-cavity sensor, making it suitable for high sensitivity pressure sensing in harsh environments. © 2014 Optical Society of America

OCIS codes: (060.2370) Fiber optics sensors; (310.6845) Thin film devices and applications.
<http://dx.doi.org/10.1364/OL.39.002827>

Fiber optic Fabry–Perot interferometric (FPI) pressure sensors have been extensively investigated and used in various areas of biomedicine, automotive industries, and environmental monitoring. Fiber optic FPI sensors have the advantages of ultra-compact size, high sensitivity, excellent thermal stability, and immunity to electromagnetic interference [1,2]. In an FPI-tip pressure sensor, the elastic diaphragm at the fiber tip is usually utilized as one of the reflecting mirrors and may be composed of silica [3–5], polymer [6], silver [7], graphene [8], or even water film [9]. Among them, all-silica FPI sensors have been proved to be the most robust and thermally stable. However, the high modulus of elasticity of silica requires a very thin diaphragm to achieve a reasonable sensitivity, and it is difficult to fabricate a smooth silica diaphragm with the thickness of less than 1 μm using conventional micromachining methods; hence, this limits the applicability of all-silica FPI sensors to low-pressure sensing applications.

In this Letter, we propose and experimentally demonstrate, an improved electrical arc discharge fabrication method to construct an all-silica FPI cavity, based on a sub-micron silica diaphragm. Such an all-silica FPI sensor exhibits a high pressure sensitivity of ~ 1036 pm/MPa at 1550 nm, which is three times larger than the formerly reported result [10,11]. Moreover, a low temperature cross-sensitivity of ~ 960 Pa/°C can also be obtained.

Figure 1 illustrates the fabrication process of the all-silica fiber sensors, which involves four steps. In step 1, as shown in Fig. 1(a), the well-cut ends of two single mode fibers (SMFs) were heated to become spherical surfaces with electrical arc discharge using a commercial fusion splicer (Fujikura-60S). The two fiber ends were then immersed into the refractive index-matching oil (from Cargille) to coat the spherical surface. In step 2, as shown in Figs. 1(b) and 1(c), using the fusion splicer, the oil-coated fiber ends were translated into alignment and spliced together with a fusion current of 18 mA and

fusion time of 1200 ms. An extrusion force was exerted to the touching region before splicing. In Fig. 1(b), d_0 denotes the moved distance of the left and right fiber ends, and d means the half-overlap of the two fiber ends at the touching region. The half-overlap d is ~ 10 μm here. Since the oil at the touching region was heated suddenly, it rapidly expanded to an air bubble. In step 3, as shown in Figs. 1(d) and 1(e), the fiber segment with the air bubble was tapered to crack by electrical arc discharge and an inner bubble was firmly formed on the fiber end. In Figs. 1(d) and 1(e), d_2 and d_3 are the moved distances of the two fiber ends during the fiber-tapering process. In step 4, as shown in Fig. 1(f), a precise electrical arc discharge, with fusion current of ~ 18 mA and fusion time of ~ 1200 ms, was repeatedly implemented at the top end of the bubble. Note that the discharge number should be less than 10 to avoid breaking the bubble. In this step, the silica wall of the bubble is melted while the air in the bubble is thermally expanded to blow up the bubble

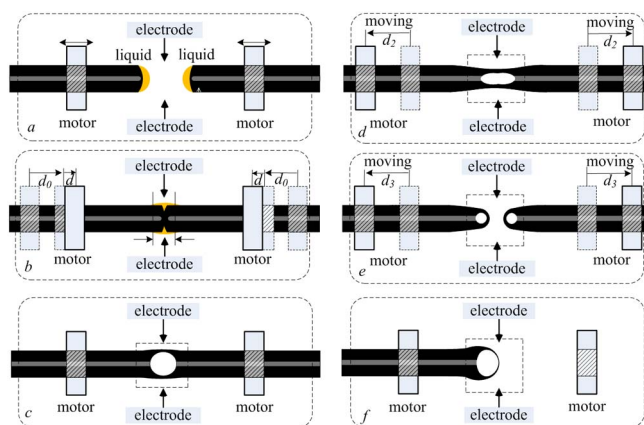


Fig. 1. Schematic diagram of the fabrication process of all-silica fiber-tip FPI sensor using electrical arc discharge assisted with oil coating in advance.

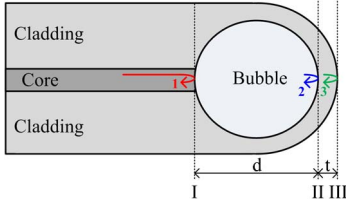


Fig. 2. Schematic diagram of the fiber-tip FPI.

and gradually reduce the thickness of the silica wall. Using this method, we have successfully fabricated an ultra-thin silica wall, with a thickness of hundreds of nanometers, which is actually a sub-micron silica diaphragm. In the whole process, we need only a common fusion splicer; there is no need for additional pressurization or wet chemical etching.

Figure 2 is a schematic diagram of this fiber-tip FPI. Three reflected waves are collected and guided back to the SMF: one is from the bubble bottom, i.e., surface-I, and the other two are from the inner and outer surfaces of the diaphragm, i.e., surface-II and surface-III.

Due to low reflectivity of the silica/air interface ($<3.5\%$), high-order FP interference could be neglected. The light intensity at the sensor output may be expressed as

$$\begin{aligned}
 I &= |E|^2 = \left| E_1 - E_2 \exp\left(\frac{4\pi}{\lambda} n_{\text{air}} d\right) \right. \\
 &\quad \left. + E_3 \exp\left[\frac{4\pi}{\lambda} (n_{\text{silica}} t + n_{\text{air}} d)\right] \right|^2 \\
 &= E_1^2 + E_2^2 + E_3^2 - 2E_1 E_2 \cos\left(\frac{4\pi}{\lambda} n_{\text{air}} d\right) \\
 &\quad - 2E_2 E_3 \cos\left(\frac{4\pi}{\lambda} n_{\text{silica}} t\right) \\
 &\quad + 2E_1 E_3 \cos\left[\frac{4\pi}{\lambda} (n_{\text{silica}} t + n_{\text{air}} d)\right] \\
 &\approx E_1^2 + E_2^2 + E_3^2 - 2(E_1 E_2 - E_1 E_3) \cos\left(\frac{4\pi}{\lambda} n_{\text{air}} d\right) \\
 &\quad - 2E_2 E_3 \cos\left(\frac{4\pi}{\lambda} n_{\text{silica}} t\right) \quad (\text{if } t \rightarrow 0), \quad (1)
 \end{aligned}$$

where E_1 , E_2 , and E_3 are the amplitudes of the three reflected waves, d is the length of bubble cavity, t is the diaphragm thickness, λ is the light wavelength, and n_{air} and n_{silica} are the refractive indices of air and silica.

Figure 3 shows the optical microscope images and the corresponding reflection spectra of the fiber-tip sensor during the process of thinning the silica diaphragm by the repeating local electrical arc discharge. Since the silica diaphragm is very thin, the modulation of the fringe envelope in Fig. 3 is regarded as the result of the interference between surface-II and surface-III. For FPI, the fringe-envelope spacing can be expressed as $\lambda^2/2n_{\text{silica}}t$.

The envelope spacings at different thinning states (states 1–5 in Fig. 3) have been measured to be ~ 76 , ~ 97 , ~ 139 , ~ 254 , and ~ 414 nm, respectively. Thus, the corresponding diaphragm thicknesses can be calculated to be ~ 8.4 , ~ 6.6 , ~ 4.7 , ~ 2.2 , and ~ 1.5 μm , respectively,

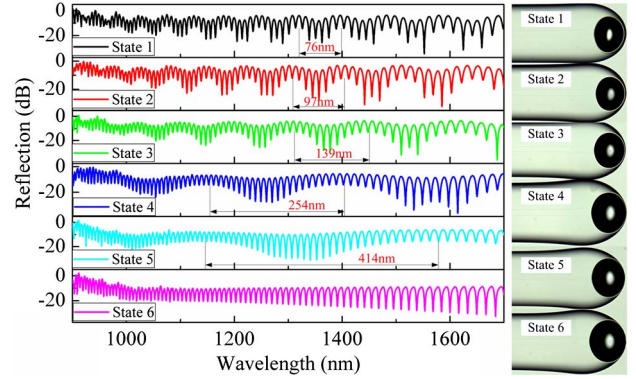


Fig. 3. Reflection spectra and optical microscope images of the fiber-tip FPI pressure sensor at different states of the diaphragm thinning process.

which agree well with the values measured from the optical microscope images.

It is difficult to observe one complete envelope from 900 to 1700 nm for state 6 in Fig. 3. To determine the manufacturing limit of the silica diaphragm thickness, the bubble was cut open using femtosecond laser micro-machining [12]. Figure 4(a) is the scanning electron microscope (SEM) image of the cut plane of the bubble. It can be seen from this figure that the inner surface is very smooth, which helps in increasing its reflectivity. Enlarged partial view of the silica diaphragm is shown in Fig. 4(b), where the diaphragm thickness is measured to be ~ 320 nm. To the best of our knowledge, it is the thinnest silica diaphragm fabricated using an electron arc discharge technique.

The experimental setup to test the proposed fiber-tip pressure sensor is illustrated in Fig. 5, where a broadband light source (BBS) and an optical spectrum analyzer (OSA) with a resolution of 0.01 nm are used, and the reflection spectrum of the sensor is measured by use of a 3-dB fiber coupler. The sensor head is placed into the gas chamber, where a commercial gas pressure generator is incorporated with a high-precision pressure meter (ConST-811) to measure the pressure in the chamber. The pressure chamber is fitted with a feed-through, sealed by strong glue to extend the fiber outside the chamber for real-time measurement.

Three samples with different diaphragm thicknesses have been tested for performance comparison. Figure 6(a) shows the reflection spectrum of the third

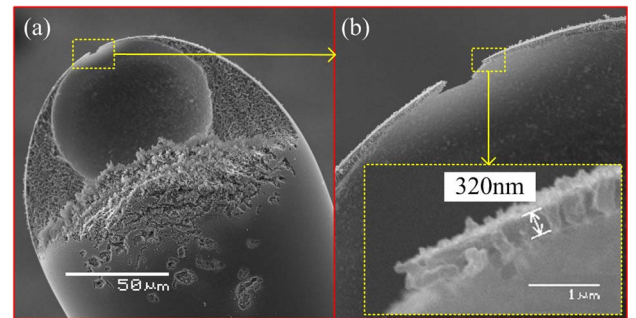


Fig. 4. (a) SEM image of the cut plane of the air bubble. (b) Enlarged partial view of the silica diaphragm at the top end of the bubble.

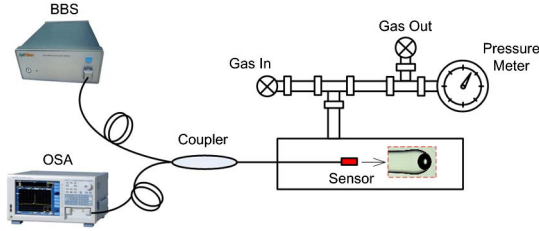


Fig. 5. Experimental setup for gas pressure measurement.

sample, i.e., S3, placed at standard atmospheric pressure and room temperature, where the fringe contrast is ~ 25 dB and the fringe spacing is ~ 12.5 nm at around 1550 nm. In the experiment, the pressure in the chamber was increased from 0 to 2.0 MPa in increments of 0.2 MPa, remaining at each step for 5 min. The reflection spectra at different pressure conditions are illustrated in Fig. 6(b), where it can be seen that, as the pressure increases, the interference dip shifts toward the shorter wavelength, with obviously decreased fringe contrast.

Fringe contrast depends on the relative optical intensity of two interference beams. The reflectivity of surface-I will hardly be changed as the pressure increases, because this surface is well protected in the fiber. Differently, the reflectivity of surface-II is very sensitive to pressure, because the increased pressure will change the flatness of diaphragm. The thinner the diaphragm is, the more significant its deflection. The change in optical intensity reflected from surface-II might result in the variation of fringe contrast. It is believed the best flatness of the diaphragm might be achieved at 0.2 MPa so that we can find an abrupt change at this pressure. To satisfy the requirements of pressure sensitivity and fringe contrast, the diaphragm thickness should be

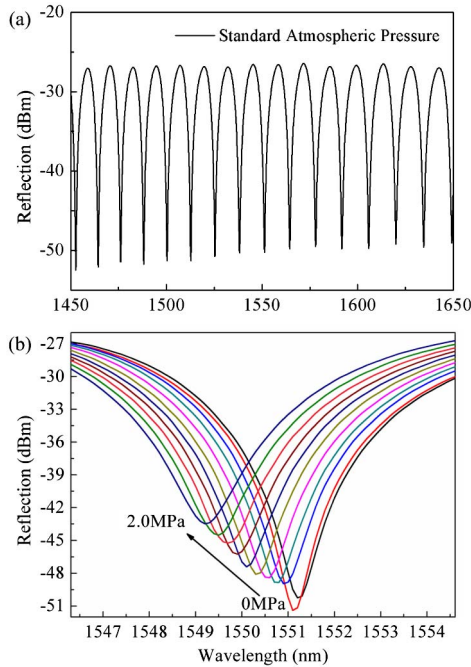


Fig. 6. (a) Reflection spectrum of the third sample, i.e., S3, at standard atmospheric pressure and room temperature. (b) Reflection spectral evolution of the sample S3 with pressure ranging from 0 to 2.0 MPa.

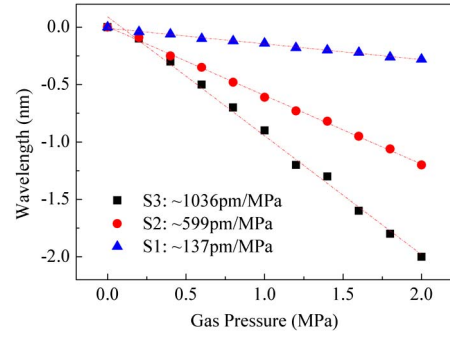


Fig. 7. Wavelength shift of the interference dip at ~ 1550 nm for the three sensor samples with the gas pressure applied.

carefully designed based on the conditions in practical measurement.

The pressure performance of three samples are compared in Fig. 7, where the pressure sensitivities can be calculated to be ~ 137 , ~ 599 , and ~ 1036 pm/MPa for the samples, i.e., S1, S2, and S3, respectively, by applying a linear fitting of the experimental data. The corresponding diaphragm thicknesses of the three samples are measured as ~ 6.7 , ~ 1.8 , and ~ 0.5 μm , respectively.

The pressure sensitivity is found to increase as the diaphragm thickness decreases, according to [10]:

$$\frac{\Delta\lambda}{\Delta P} = \frac{(1-\nu)\lambda R^2}{2Edt}, \quad (2)$$

where ν is Poisson's ratio, λ is the dip wavelength, R is the radius of bubble, E is Young's modulus of silica, d is the length of bubble cavity, and t is the diaphragm thickness. The thinnest silica diaphragm in previous reports is 2.2 μm , with the corresponding sensitivity of 315 pm/MPa [10]. Note that the measured sensitivity is not a perfect linear relationship inverse of the diaphragm thickness. In Eq. (2), the bubble is regarded as a thin sphere shell, with a uniform silica wall; in reality, however, the silica wall is not uniform and the central part is much thinner than the surrounding area. The nonuniformity of the wall thickness could result in this nonlinear response.

A simulation model is established in ANSYS to investigate the diaphragm deformation with an increase of pressure. Figure 8(a) shows the simulated deformation of the diaphragm with a thickness of ~ 0.5 μm at 1.0 MPa,

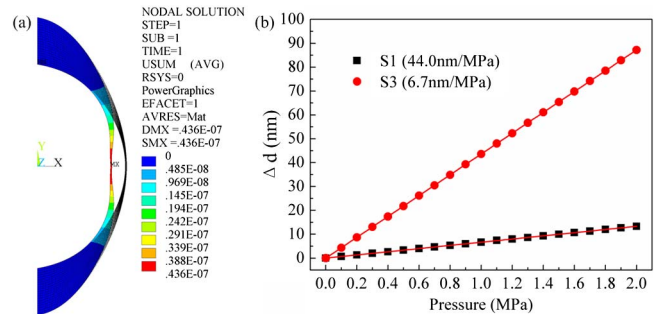


Fig. 8. (a) Simulation model of the diaphragm deformation with increasing pressure. Young's modulus of silica is 73 GPa; Poisson's ratio is 0.17; silica density is 2700 kg/m^3 . (b) Simulated relationship between the value of the diaphragm deformation and the applied pressure.

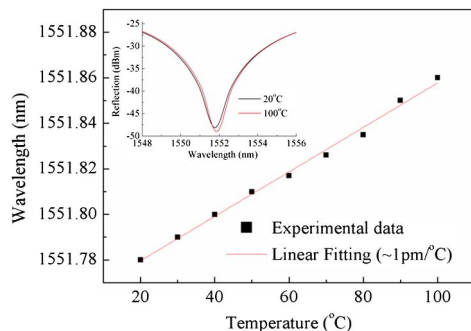


Fig. 9. Linear relationship between the wavelength shift of the interference dip at ~ 1550 nm for sample S3 and ambient temperature. Inset: reflection spectra of sample S3 at 20°C and 100°C .

where the deformation value of different parts is displayed in the note. Using this method, the relationship between the applied pressure and the diaphragm deformation, i.e., the length change of bubble cavity Δd , can be simulated, and the simulation result is shown in Fig. 8(b), where the slopes for the samples S1 and S3 are 6.7 and 44.0 nm/MPa, respectively. The simulated sensitivity of S3 is nearly 7 times larger than that of S1, which agrees well with the experimental result.

Besides reducing the diaphragm thickness, another way to enhance pressure sensitivity is to increase the radius of the bubble. By reducing the diaphragm thickness, the sensor will be compact in size, but its mechanical strength becomes weaker, especially when the diaphragm thickness is less than $1\ \mu\text{m}$. By increasing the bubble radius, the mechanical strength of sensor is good; however, the increased device size may limit its applications in some precise measurements. The selection of a sensitivity-enhancement method depends on the practical sensing requirements.

The influence of temperature on the fiber sensor has been investigated by placing the device in an electrical oven and gradually increasing the temperature from room temperature to 100°C in increments of 10°C [13–15]. Each tested temperature was maintained for 10 min. The inset of Fig. 9 shows the reflection spectra of the sample S3 at 20°C and 100°C , and a redshift is clearly observed when the temperature is increased. Wavelength shift of the interference dip at ~ 1550 nm with temperature variation is displayed in Fig. 9, where a linear relation is found and the temperature sensitivity obtained is $\sim 1\ \text{pm}/^\circ\text{C}$. Temperature response of the fiber sensor results from the thermal expansion of the silica bubble. When no temperature compensation is employed in practical measurement, the error resulting from temperature cross-sensitivity is $\sim 960\ \text{Pa}/^\circ\text{C}$, which could be neglected in the large pressure measurement.

In conclusion, we have experimentally demonstrated a sub-micron silica diaphragm-based fiber-tip FPI for high pressure sensitivity measurement. The ultra-thin silica diaphragm is fabricated using an improved electrical arc discharge technique and the thinnest diaphragm achieved is $\sim 320\ \text{nm}$, which might be the thinnest silica diaphragm fabricated by the electron arc discharge method. Pressure response of the fiber FPI sensor has been investigated and the one with a diaphragm thickness of $\sim 500\ \text{nm}$ exhibits the highest pressure sensitivity of $\sim 1036\ \text{pm}/\text{MPa}$. Moreover, such a fiber sensor shows a low temperature cross-sensitivity of $\sim 960\ \text{Pa}/^\circ\text{C}$. The sub-micron silica diaphragm-based fiber-tip FPI sensors have the advantages of low fabrication cost, high mechanical strength, relatively high pressure sensitivity and low temperature cross-sensitivity, and are promising for high sensitivity pressure sensing in harsh environments.

This work was supported by the National Natural Science Foundation of China (Nos. 11174064, 61308027, 61377090), National Science Foundation of SZU (No. 00036401), Science & Technology Innovation Commission of Shenzhen (Nos. KQCX20120815161444632 and JCYJ20130329140017262), Distinguished Professors Funding from Shenzhen University and Guangdong Province Pearl River Scholars.

References

1. Y. J. Rao, *Opt. Fiber Technol.* **12**, 227 (2006).
2. Y. Wang, D. N. Wang, W. Jin, and X. Fang, *IEEE J. Quantum Electron.* **42**, 868 (2006).
3. D. Donlagic and E. Cibula, *Opt. Lett.* **30**, 2071 (2005).
4. Y. Z. Zhu and A. B. Wang, *IEEE Photon. Technol. Lett.* **17**, 447 (2005).
5. W. H. Wang, N. Wu, Y. Tian, C. Niezrecki, and X. W. Wang, *Opt. Express* **18**, 9006 (2010).
6. H. Bae and M. Yu, *Opt. Express* **20**, 14573 (2012).
7. G. Guo, T. Fink, M. Han, L. Koester, T. Turner, and J. Huang, *Opt. Lett.* **37**, 1505 (2012).
8. J. Ma, W. Jin, H. L. Ho, and J. Y. Dai, *Opt. Lett.* **37**, 2493 (2012).
9. Y. Wang, D. N. Wang, C. Wang, and T. Y. Hu, *Opt. Express* **21**, 14084 (2013).
10. J. Ma, J. Ju, L. Jin, and W. Jin, *IEEE Photon. Technol. Lett.* **23**, 1561 (2011).
11. C. Liao, T. Y. Hu, and D. N. Wang, *Opt. Express* **20**, 22813 (2012).
12. C. Liao, L. Xu, C. Wang, D. N. Wang, Y. Wang, Q. Wang, K. Yang, Z. Li, X. Zhong, J. Zhou, and Y. Liu, *Opt. Lett.* **38**, 4473 (2013).
13. Y. Rao, X. Zeng, Y. Zhu, Y. Wang, T. Zhu, Z. Ran, L. Zhang, and I. Bennion, *Chin. Phys. Lett.* **18**, 643 (2001).
14. Y. Wang, L. Xiao, D. N. Wang, and W. Jin, *Opt. Lett.* **31**, 3414 (2006).
15. C. Liao, D. N. Wang, Y. Li, T. Sun, and K. T. V. Grattan, *Appl. Opt.* **48**, 3001 (2009).